Reconstruction of the Virtual Geomagnetic Pole (VGP) path at high latitude for the last 22 kyr: the role of radial field flux patches as VGP attractor.

Chiara Caricchi [1*], Saioa A. Campuzano[2], Leonardo Sagnotti [1], Patrizia Macrì [1], Renata G. Lucchi [3-4]

1 Istituto Nazionale di Geofisica e Vulcanologia (INGV), Via di Vigna Murata 605, I-00143, Rome, Italy

2 Instituto de Geociencias IGEO-CSIC, C/ Doctor Severo Ochoa 7. 28040, Madrid, Spain

3 Istituto Nazionale di Oceanografia e di Geofisica Sperimentale (OGS), Borgo Grotta Gigante 42/c, I-34010, Sgonico (TS), Italy

4 Centre for Arctic Gas Hydrate, Environment and Climate (CAGE), UiT- The Arctic University of Norway, Tromsø, Norway

*corresponding author: chiara.caricchi@ingv.it

Abstract

Reconstruction of geomagnetic field changes has a strong potential to complement geodynamo modeling and improve the understanding of Earth's core dynamics. Recent works based on geomagnetic measurements pointed out that over the last two decades the position of the north magnetic pole has been largely determined by the influence of two competing flux lobes under Canada and Siberia.

In order to understand if the waxing and waning of magnetic flux lobes have driven the path of geomagnetic paleopoles in the past, we present an augmented and updated record of the chronology and paleosecular variation of geomagnetic field for the last 22 kyr derived from sedimentary cores

collected along the north-western margin of Barents Sea and western margin of Spitsbergen (Arctic). The path of the virtual geomagnetic pole (VGP) has been reconstructed over this time period and compared with the maps of the radial component of the geomagnetic field at the core-mantle boundary, obtained from the most recent models. The VGP path includes centuries during which the VGP position is stable and centuries during which its motion accelerates. We recognize both clockwise and counterclockwise VGP paths, mostly developing inside the surface projection of the inner core tangent cylinder in the Arctic region. The VGP path seems to follow the appearance of B_r patches of normal magnetic flux, especially those located under Siberia and Canada areas, but also those that may cause peculiar paleomagnetic features such as the Levantine Iron Age Anomaly.

Keywords

Geomagnetic paleosecular variation; Relative paleointensity; Flux lobes; Levantine Iron Age Anomaly; Marine sediment cores; Arctic region

1 Introduction

Reconstruction of geomagnetic field changes has a strong potential to complement geodynamo modeling and improve the understanding of Earth's core dynamics (Panovska et al., 2018 and reference therein). There is potential social relevance of the paleosecular variation (PSV) reconstruction, as demonstrated by the fact that in 2019 the World Magnetic Model, used for navigation, was updated a year in advance, as a consequence of the recent acceleration of north magnetic pole motion, see Livermore et al., (2020). The authors highlighted that over the past 50 years the north magnetic pole has traveled along a linear path that connects two patches of strong radial magnetic field (B_r) at the Core-Mantle Boundary (CMB) centered at high latitudes under Canada and Siberia. The time-dependent position of the pole along this path is related to a balance between the competing influences of the Canadian and Siberian geomagnetic flux lobes at the CMB. A decrease of the Canadian flux patch and a slight intensification of the Siberian flux patch cause an

acceleration of the magnetic pole path toward Siberia. Did this relationship between the waxing and waning of geomagnetic flux lobes and the pole position occur also in the past? To answer this question, it is necessary to focus on indirect geomagnetic observations, such as those inferred from paleomagnetic measurements and analyses. The principal sources of paleomagnetic data are volcanic rocks, lake and marine sediments, and archeological artifacts. In the last decades, paleomagnetic data have been widely used to reconstruct the past geomagnetic field at different temporal and spatial scales. Several models have been produced, especially for the Holocene, constraining the morphology and variability of geomagnetic field at relatively high resolution (Constable et al., 2000, 2016; Campuzano et al., 2019; Donadini et al., 2009; Johnson and Constable 1995, Korte and Constable 2003, 2005; Korte et al., 2005, 2009; Korte and Holme, 2010; Nilsson et al., 2014; Osete et al., 2020; Pavón-Carrasco et al., 2009, 2010, 2014; Panovska et al., 2018 among others).

Some of these models analyze the presence of flux patches at the CMB in the northern hemisphere. Pavón-Carrasco et al. (2014) studied the last 14000 years from SHA.DIF.14k, a global geomagnetic field model based on archeomagnetic and volcanic data. For the last 9000 years, they highlighted the appearance of marked lobes of magnetic flux in high latitudes when the dipole moment was maximum. When the dipolar field decreased, a rupture of this dipolar pattern was observed and a weakened magnetic flux patches in the northern hemisphere with the appearance of new lobes in lower latitudes with low (or even reversed) values of B_r.

The new model SHAWQ-Iron Age by Osete et al. (2020) that spans from 3300 to 2000 BP improves the description of the evolution of the Levantine Iron Age Anomaly (LIAA) formerly observed by several authors in the Levantine region and later in the Mediterranean region (e.g. Shaar et al., 2016, 2017; 2018; Davies and Constable, 2017; Beguin et al., 2019; Rivero-Montero et al., 2021). According to Osete et al. (2020), the LIAA is related to a normal flux patch at the CMB below Arabian Peninsula, which was observed starting from around 2950 BP. After its appearance, it expanded towards the north-west and around 2600-2500 BP stationed under the European continent and then disappeared in situ. Rivero-Montero et al. (2021) however do not observe a clear westwards migration

of the LIAA event and propose that the maximum geomagnetic intensity around 2500 BP occurred in a large region, from Western Europe to Turkey, at the same time. This recent result agrees with Davies and Constable (2017) work, who stated that this kind of feature could have originated from the CMB only in the case that its effect at Earth's surface was observed in a region >60°.

How does the appearance and disappearance of these flux patches impact the VGP motions at high latitudes? To investigate these issues, we reconstructed the geomagnetic field PSV for the last 22.2 calibrated kiloyears before the present (cal kyr BP_{2000}, with "present" fixed at 2000 CE) analyzing paleomagnetic and rock magnetic data from sedimentary cores collected from the north-western margin of the Barents Sea and western margin of Spitsbergen (Arctic). These paleomagnetic records might extend back in time the known information about the geomagnetic field variation in the recent geological time and provide constraints for the development of regional (Arctic) and global models of geomagnetic field variation.

Starting from paleomagnetic declination and inclination stack curves, the VGP path has been reconstructed and compared with maps of the radial component of the geomagnetic field at the CMB calculated using different global geomagnetic field reconstructions: GGF100k (Panovska et al., 2018), CALS10k.2 (Constable et al., 2016), SHAWQ-Iron Age (Osete et al., 2020) and SHAWQ2k (Campuzano et al., 2019).

2 Study Area and materials

The sedimentary cores, taken into account in this work, were recovered along the north-western margin of Barents Sea and western margin of Spitsbergen during the past years in the framework of several international research projects (Table S1).

In brief, the morphology of these continental margins was shaped by a series of advances and retreats of the Svalbard-Barents Sea ice sheet related to the Late Quaternary climatic changes (Patton et al., 2017). The paleo-ice stream produced deep erosion moving along cross-shelf glacial troughs (e.g. Kveithola and Storfjorden troughs), and massive deposition on the continental slope, resulting in the

buildup of seaward-convex slope-aprons called Trough Mouth Fans (TMFs) (Pedrosa et al, 2011; Mattingsdal et al., 2014; Lucchi et al., 2013; Rebesco et al., 2013). In addition to glacigenic processes, the margin is characterized by persistent bottom currents flowing along the slope (contour currents, Jakobsson et al., 2007; Poirier and Hillaire-Marcel, 2011 among others). These currents are responsible for the development of sediment drifts in the areas shielded from direct glacigenic input, such as the Bellsund and Isfjorden drifts identified along the western continental margin of Svalbard (Rebesco et al., 2013). The studied sediment cores were collected in areas mainly affected by contouritic deposition:

- Calypso cores GS191-01PC and GS191-02PC, collected from the Bellsund and Isfjorden drifts, respectively.
- Piston core SV-04 and gravity cores EG-02 and EG-03 collected from the Storfjorden TMF.
- Gravity core GeoB17603-3 from the Kveithola TMF.

The cores were previously analyzed using a multidisciplinary approach (Lucchi et al., 2012, 2013, 2015; Sagnotti et al., 2011a and Caricchi et al., 2018, 2019) including Accelerator Mass Spectrometry (AMS) ^{14}C dating, lithofacies analysis, paleomagnetic and rock magnetic analyses.

In this work we refined the initial chronologies and core correlations as described in the next section.

3 Cores correlation and refining age models

3.1 Cross-core correlations

High-resolution core correlations were established comparing rock magnetic and paleomagnetic stratigraphic trends, by means of the StratFit software (Sagnotti and Caricchi, 2018). The correlation process is based on the Excel FORECAST function which implies a linear regression between subsequent pairs of selected tie-points. By doing this, it is possible to estimate the equivalent stratigraphic depth of the correlated curve in the depth scale of a selected master curve.

In this work, core GS191-01PC has been selected as the master curve (due to the higher number of age and lithological constraints) and the equivalent depth of SV-04, EG-02, EG-03, GeoB17603-3

and GS191-02PC (correlated curves) was then computed with StratFit. The choice of the tie-point pairs has been made taking into account the lithofacies (Lucchi et al., 2013; Caricchi et al., 2018, 2019), significant and coincident peaks and troughs of the curves of rock magnetic and paleomagnetic parameters (Sagnotti et al., 2011a; Caricchi et al., 2018, Caricchi et al., 2019), and the previously published age models (Sagnotti et al., 2011a; Caricchi et al., 2018, 2019, 2020). In figure 1 the correlation of the Anhysteretic Remanent Magnetization (ARM) stratigraphic trends (see Sagnotti et al., 2011a; Caricchi et al., 2018, 2019 for additional details about ARM parameters and their downcore variations) is shown as a representative example for the output of the high-resolution core correlation procedure.

The ARM curves of the correlative cores match closely that of the master core, as visualized in the graphs and testified by the correlation coefficients ($R>0.75$; Fig.1).

This correlation among cores collected far from each other and distributed along a 330 km-long transect crossing the north-western margin of the Barents Sea and western margin of Spitsbergen, allowed us to correlate paleoclimatic events along the entire margin and to obtain a new piece of knowledge that can be used as a benchmark for the reconstruction of the paleoclimatic evolution of this region.

In addition, the improvement of the cross-core correlation also allowed us to refine the formerly published age models, as reported in detail below.

3.2 Refined age models

The age model of the cores was originally established by taking into account the variation of the RPI, the paleomagnetic inclination and declination curves, the lithological constraints and the radiocarbon ages, which provided the main chronologic tie-points (Caricchi et al., 2019; 2020). For a second-order chronology refinement, in this study we also considered the results from the cross-core correlation process. Then, each core paleomagnetic record was also correlated with the most recent paleomagnetic stack curves and models. In particular, GICC05-GLOPIS75 has been taken into

156 account because this stack benefits from the correlation of the ^{10}Be and ^{36}Cl records from the
157 Greenland ice cores with GLOPIS-75. This correlation allows to precisely assess the rates of change
158 of the field intensity during periods of large directional changes (i.e., the Laschamp and Mono Lake
159 excursions) and during periods when a large decrease of the dipolar field intensity occurred without
160 being associated with significant directional changes (Laj and Kissel, 2015). The use of
161 paleomagnetic constraints in the correlation must be taken into account for global paleofield modeling
162 purposes.
163 For this latter correlation, the target curves from stacks and models were computed at the EG-03 core
164 location, which has been chosen as the reference location due to its central position in the study area.
165 Regarding the RPI curves, for all cores we considered the RPI computed from the NRM/ARM ratio
166 with the exception of the core GeoB17603-3, for which we used the RPI computed from the NRM/k
167 ratio. The poor efficiency of the NRM/ARM normalization with respect to the NRM/k normalization,
168 in this latter core, is attributed to the effects of diagenetic dissolution in the upper part of the
169 sedimentary sequence, that caused a preferential depletion of fine-grained ferromagnetic minerals
170 (which affects ARM intensity more than magnetic susceptibility k).
171 Correlation between paleomagnetic trends and target curves was accomplished by the StratFit
172 software (Sagnotti and Caricchi, 2018), transferring records to a common age scale using the same
173 method employed for cross-core correlation.
174 In order to compare data with different ranges of variation (e.g., RPI curves and models) we adopted
175 the normalization method reported in the Supplementary Material (Appendix A). The intensity of the
176 geomagnetic field, for the curves from geomagnetic models (e.g. GGF100k) and for GICC05-
177 GLOPIS75, was rescaled only for the time interval overlapping the one spanned by the analyzed
178 cores.
179 We point out that the paleomagnetic data for the time interval older than the Holocene for the EG-02,
180 EG-03 and SV-04 cores are presented here for the first time.

Table S1 in supplementary material lists all the data, for each core, referred to the formerly published age models (Caricchi et al., 2019; 2020) and the newly refined age models.

3.2.1 GS191-02PC and GS191-01PC cores

These cores were compared with the reference RPI stack GICC05-GLOPIS75 (Laj and Kissel, 2015) and GGF100k model (Panovska et al., 2018) (Table S1, Fig. S1). This procedure allowed us to refine the age model for the older portion of the GS191-02PC between 11 and 17 m (Caricchi et al., 2019). The maximum age adjustment was for the core interval 13-16 m, which resulted in a shift in age of 2-3 kyr (Table S1, Fig. 2, Fig. S1a, b). The age model of GS191-01PC (Caricchi et al., 2019) was refined for the Holocene interval between 5 and 10 cal kyr BP_{2000} (2.14 – 5.89 m) with a maximum age shift of 123 yr (Table S1, Fig. 2, Fig. S1c, d).

3.2.2 EG-03 and EG-02 cores

These cores were compared with the CALS10k.2 (Constable et al., 2016) and SHA.DIF.14k (Pavón-Carrasco et al., 2014) models (Table S1, Fig. 2, Fig. S2).

For the EG-03 we refined the portion of the core between 1.4 and 2.6 m, with a maximum age shift of 950 yrs around 2.3 m (Table S1, Fig. 2, Fig. S2a, b). The age model of the EG-02 core was refined for the portion from 0.23 to 1.40 m with major adjustments of age shift 900 yrs between 0.35 and 0.45 m and 300-400 yrs between 1.30 and 1.40 m (Table S1, Fig. 2, Fig. S2c, d).

3.2.3 SV-04 core

SV-04 core was compared with RPI stack GICC05-GLOPIS75 (Laj and Kissel, 2015), GGF100k (Panovska et al., 2018), CALS10k.2 (Constable et al., 2016) and SHA.DIF.14k (Pavón-Carrasco et al., 2014) models (Table S1, Fig. 1, Fig. S3). We refined the age model for the interval depth between 1.01-1.57 m, with a maximum age shift of 800 yrs around 1.53 m. The new age models are now consistent with the identification of the Melt Water Pulse (MWP)-19ka (e.g Clark et al. 2004) and Heinrich event H-2 (e.g. Hemming 2004) as indicated by the lithological and compositional characteristics of sediments.

4 Geomagnetic field reconstruction

Paleomagnetic data from the cores were merged in a stack curve for the characteristic remanent magnetization (ChRM) declination and inclination (Fig. 3a,b), considering three main time intervals: i) 0.6-10 cal kyr BP_{2000}; ii) 10-14 cal kyr BP_{2000}; iii) 14-22.2 cal kyr BP_{2000}.

In detail, for the time range i) we used the data from the EG-02, EG-03, SV-04 and GeoB17603-3 cores; data from the cores collected in the sediments drift (GS191-01PC, GS191-02PC) were not used because of the poor quality of the paleomagnetic signal in the Holocene portion, which was probably affected by diagenetic dissolution of ferromagnetic minerals (Caricchi et al., 2019). For the time range ii) we used data from all the six cores. Only the data from the cores spanning older age intervals (SV-04, GS191-01PC, GS191-02PC) were used for the iii) time interval.

For the stacking process, paleomagnetic directions were grouped with an age sliding window of 200 yr from present-day up to 14 cal kyr BP_{2000}. The paleomagnetic directions within the 14 – 22.2 cal kyr BP_{2000} time range were grouped with an age sliding window of 600 yr (Fig. 3c). This procedure was necessary to ensure a number of data (N) higher than 5 for all the steps in the age interval 0.6 - 22.2 cal kyr BP_{2000} (Fig. 3c) and led to a different time resolution in the two time intervals.

The obtained PSV stack for paleomagnetic declination and inclination, called the NBS22.2k stack, was defined by computing a mean paleomagnetic direction for each time interval using Fisher statistics (Fisher, 1953).

Likewise, the NBS22.2k RPI stack curve was defined using the RPI data from the same cores. In this case, the arithmetic mean has been computed for the RPI data falling within sliding windows with the same spacing (200 and 600 yr) used for the PSV data (Fig. 4).

Afterward, the NBS22.2k PSV and RPI stack curves have been compared with the PSV and RPI variations expected according to the geomagnetic field models: CALS10k.2 (Constable et al., 2016); SHA.DIF.14k (Pavón-Carrasco et al., 2014); SHAWQ-Iron Age (Osete et al., 2020); SHAWQ2k (Campuzano et al., 2019); GGF100k (Panovska et al., 2018). The NBS22.2k RPI stack curve was also compared with the GICC05-GLOPIS75 stack curve (Laj and Kissel, 2015) (Fig. 5).

For this comparison, we also normalized all the curves by the method reported in the Supplementary Material (Appendix A) (Fig. 5). The NBS22.2k RPI stack is in general agreement with the models and GICC05-GLOPIS75 for the first 15 kyrs, with the exception of the SHA.DIF.14k around 11kyr, which shows a minimum in intensity not observed in the other models. SHAWQ family models show exaggerated minima at present-day and at about 2 and 3 cal kyr BP_{2000}. This is an artifact due to the normalization method and it is related to the fact that the SHAWQ family models have a much higher median value than other models extending to older periods, since in the last 3.3 kyr BP_{2000} the magnetic field was characterized by intensity values distinctly higher than for the older interval from 3.3 kyr BP to 10 kyrs BP_{2000}.

It is also evident a slight offset between the GGF100k model and the GICC05-GLOPIS75 that became more accentuated after 14 kyr. We can assume that this is related to the fact that spherical harmonic models provide regional predictions including non-axial-dipole contributions while the stack has attempted to average those out using a wide spatial distribution of records. Moreover, GGF100k and GICC05-GLOPIS75 used different records and potentially inconsistent time scales.

NBS22.2k inclination and declination curves show a really good match with the trends computed according to the models for the time interval between 14 cal kyrs BP_{2000} and Present. A mismatch with the GGF100k model became evident in the interval between around 14 and 18 cal kyr BP_{2000}. The sharp declination change and the inclination almost vertical between 2.6 and 2.4 cal kyr BP_{2000} (a time interval coeval with the LIAA) is a peculiar feature related to the fact that the VGP in this time period passed close to the cores position (see also Fig. 6) and accelerated its motion. A similar feature was also observed by Turner and Thompson (1981) in their pioneering study of PSV from lake sediments in Britain and named as “f-e event”. This event has also been recognized in various paleomagnetic records from southern Europe (e.g., Sagnotti et al., 2011b).

5 The VGP paths during the last 22.2 cal kyr BP_{2000}

We reconstructed the Virtual Geomagnetic Pole (VGP) path for the last 22.2 cal kyr BP_{2000} on the basis of the declination and inclination values of the NBS22.2k PSV stack curves, following the method by Noel and Batt (1990). The reconstructed VGP paths have been plotted in figure 6 according to six consecutive age intervals: i) 22.2 – 15 cal kyr BP_{2000} (Fig. 6a); ii) 15 – 11.8 cal kyr BP_{2000} (Fig. 6b), iii) 11.8 – 9.0 cal kyr BP_{2000} (Fig. 6c), iv) 9.0 – 6.2 cal kyr BP_{2000} (Fig. 6d), v) 6.2 – 3.2 cal kyr BP_{2000} (Fig. 6e), vi) 3.2 – 0.6 cal kyr BP_{2000} (Fig. 6f). The VGP moved mostly inside the surface projection of the inner core tangent cylinder, which intersects the Earth's surface at ca. ±69.5 of latitude, with a few exceptions: 1) from 15.8 to 15.4, 2) around 5.6 and 3) 3.2 cal kyr BP_{2000}. Moreover, the VGP path traced both clockwise and counterclockwise trajectories. For some centuries the VGP position was substantially stable, whereas for others it significantly accelerated its motion with rapid variations and large deviations from the position of a geocentric axial dipole (GAD).

In Figure 6g, the rate of change of the VGP path has been calculated as the distance covered by the VGP between two consecutive times (in degrees per yr). We also computed the mean and standard deviation of the rate of change for different time intervals; the periods between 14 and 22.2 cal kyr BP_{2000} and 8 and 10 cal kyr BP_{2000} show the lowest standard deviation, with values lower than 0.01 °/yr. This means that the rate of change for these periods is less variable. It is important to consider that for the older ages this could be due to a lower resolution, since the estimation of the VGP rate of change was calculated using a sliding window of 600 yrs. Future studies could help to better define this time interval. In the other time intervals, highlighted with braces in Figure 6g, the standard deviation is greater than 0.01 °/yr, reaching values up to 0.02 °/yr in the most recent period (0.6-3 cal kyr BP_{2000}). This means that the rate of change is more variable for these periods. It is worth noting that the maximum rate of change of the VGP occurs at the end of a sharp acceleration event during the Levantine Iron Age Anomaly times (3000 – 2700 BP, Shaar et al., 2016), terminating around 2.1 cal kyr BP. This increase of the rate of change could be due to the appearance of a third flux lobe in the Atlantic region, as observed in CALS10k.2 model, and the associated increased radial flux at low to mid latitudes in the Pacific (see Fig. S4 in the Supplementary Material). This pattern is however

not well observed in the SHAWQ-Iron Age model. The analysis of the rate of change also points out an increase in the mean rate of change in the most recent times, with a value of around 0.05 º/yr for the period from 0.6 to 3.0 cal kyr BP_{2000}. In the rest of the record the mean rate of change oscillates between 0.01 and 0.03 º/yr. We will discuss in detail the time intervals with higher rates of change and standard deviation below. For a comparison with the rate of change of VGP using geomagnetic field models for different maximum harmonic degree see Figure S5 in the Supplementary Material.

As pointed out in Caricchi et al. (2020), the VGP path is possibly related to the time variability and temporary occurrence of geomagnetic radial field flux patches in the northern hemisphere, which seems to have the function of a VGP attractor. The hypothesis is that when the paleopole changes sharply its movement (in terms of position, path and/or velocity), this is due to the rapid (hundred years or less) evolution of B_r patches at the CMB, which appear or disappear, weaken or intensify and are commonly related to a significant contribution of the non-dipole magnetic field components (Fig. S6).

In order to verify this hypothesis, we computed the B_r at the CMB since 14 cal kyr BP_{2000}, using different models for different time intervals. The following models have been taken into account:

i) The GGF100k for the time interval between 14 and 10 cal kyr BP_{2000} (Fig. S7)

ii) The CALS10k.2 for the interval between 8.0 and 3.4 cal kyr BP_{2000} (Fig. S8)

iii) The SHAWQ-Iron Age for the time interval between 3.0 to 2.2 cal kyr BP_{2000} (Figs. 7 and 8)

iv) The SHAWQ2k for the time interval between 1.8 to 0.6 cal kyr BP_{2000} (Fig. 8)

We have not used the SHA.DIF.14k model because it spans the same time interval as the CALS10k.2 and SHAWQ family, which are more recent.

In detail, the B_r at the CMB has been calculated from the Gauss coefficients of the geomagnetic field models up to maximum harmonic degree 6 to avoid the effect of shorter time scales of the higher degrees, which are poorly resolved and affected by model parametrization. We calculated the B_r

values in a regular grid of 5,000 points around the world, by adding other additional 1,000 points within the Arctic circle to better constrain the grid at high northern latitudes.

The analysis confirmed that the VGP trajectory was driven by the temporary occurrence of normal B_r flux patches, as formerly suggested in Caricchi et al. (2020). This effect is particularly evident for the last 10 cal kyr BP_{2000} but it can be now extended back to the past. To help with the interpretation of the results, we have selected the normal flux patches (NFPs) that act as VGP attractors according to our interpretation. To do that, we have chosen different contour lines to highlight the most relevant and persistent NFPs for every time interval analyzed. The used contour levels are specified in the corresponding figure captions (see Figs. 7, 8 and S7 and S8 in the Supplementary Material). The selected NFPs have been marked with a white contour line in order to improve the visualization.

In order to quantify the NFPs effect over the VGP path, we have calculated the Flux Concentration Factor (FCF) (Eq.4 in Christensen et al., 2010). Based on the idea of the waxing and waning of radial magnetic flux lobes between Siberian and Canadian hemispheres, we calculated the global FCF and the FCF in northeastern hemisphere (Siberian region) and northwestern hemisphere (Canadian region) considering only normal magnetic flux (B_r<0 nT) and compared these estimates with the VGP positions to better evaluate if the normal flux concentrations attract the VGP positions. For the Siberian or northeastern hemisphere we use latitudes >= 0ºN and longitudes [0,180]ºE. For the Canadian or northwestern hemisphere we use latitudes >= 0ºN and longitudes [0,180]ºW. Results are summarized in Table S2 in the Supplementary Material. The FCF is a measurement of the flux concentration. According to Christensen et al. (2010), the maximum global FCF values are obtained when the flux emerges at a very concentrated place and penetrates uniformly over the rest of the globe, and FCF approaches zero when the flux emerges uniformly in one hemisphere and penetrates uniformly in the other hemisphere. For a purely dipolar field the global FCF is 0.8. If we observe global FCF values in Table S2, at 8.0 cal kyr BP_{2000} it is almost dipolar while at 3.0 cal kyr BP_{2000} it presents the highest values of FCF. It corresponds with the occurrence of the "Levantine Iron Age Anomaly" (see below for further details). Regionally, it might be expected that regions with higher

335 values of FCF attract more the VGP because they represent zones with higher flux concentration.
336 High values of FCF can be also obtained as a result of multiple areas of concentrated flux.
337 Focusing on VGP path from NBS22.2k stack (red curve in Figs. 7, 8 and S7, S8) we notice that the
338 VGP bounced back and forth between the Arctic Canadian and Siberian shorelines; around 14 cal kyr
339 BP_{2000} the paleopole was at high latitude near Canada and Alaska. Afterward, with a clockwise
340 motion it moved toward Siberia (Siberian FCF > Canadian FCF, Table S2), possibly attracted by a
341 flux patch that showed up at 13.4 cal kyr BP_{2000} in the area close to the Kola Peninsula. After, with a
342 clockwise rotation the paleopole moved toward the Arctic Canadian and then returned toward the
343 Russian shoreline of the Arctic Sea at 12.4 cal kyr BP_{2000}, possibly attracted by the flux patch below
344 Russia (Siberian FCF > Canadian FCF). At 12.0 cal kyr BP the VGP returned toward Canada (Fig.
345 S7). This movement is not well captured by FCF values as Siberian FCFs are higher than the Canadian
346 one. However, we see a slight increase of Canadian FCF around 12.0 cal kyr and a NFP emerging in
347 the Quebec region that is completely formed at 11.0 cal kyr BP_{2000} when the VGP is close to it. It is
348 then observed a VGP movement towards Siberia up to 10.0 cal kyr BP_{2000}, which corresponds with
349 an increase of FCF values in the Siberian/Northeastern hemisphere. The VGP path kept the same
350 behavior during the time interval between 10.0 and 3.4 cal kyr BP_{2000} (Fig. S8). The more persistent
351 the flux lobes were, the longer the VGP stationed in the same position. We also notice that when FCF
352 is higher in the Canadian or Siberian hemisphere, the movement of the VGP is towards them (Table
353 S2). At around 3.2 cal kyr BP_{2000} the paleopole moved sharply toward relatively low latitudes and at
354 longitudes between two flux lobes between Canada and Siberia (although it is worth to mention that
355 Canadian FCF > Siberian FCF at 3.2 cal kyr BP_{2000}). This displacement towards low latitudes could
356 be due to the development of a NFP in the Levantine area and related to the "Levantine Iron Age
357 Anomaly" (see below for more details).
358 From 3.0 to 2.6 cal kyr BP_{2000} the paleopole stationed at relatively low latitude (offshore Norway;
359 Fig.7) possibly attracted by an already clearly formed low latitude flux patch, in association with the
360 "Levantine Iron Age Anomaly" (LIAA). This anomaly is related to a normal flux patch at the CMB

361 below the Arabian Peninsula, which appeared around 3.0 cal kyr BP, as highlighted by Osete et al.
362 (2020). After reaching its highest value at around 2.95 cal kyr BP the flux patch expanded toward
363 NW (Osete et al., 2020, Rivero-Montero et al., 2021), and the VGP moved in the same direction
364 (Fig.7). This fact is especially remarkable because this B_r patch emerged from low latitudes. This
365 finding can mean that either 1) this kind of strong geomagnetic anomalies due to the development of
366 B_r patches at low-middle latitudes have a global effect on the VGP path, or 2) our sedimentary cores
367 were affected by a regional geomagnetic effect, since they were close enough to the B_r patch.
368 After the flux patch related to the LIAA anomaly vanished in situ around 2.35 cal kyr BP (Osete et
369 al., 2020), the VGP started to move clockwise toward higher latitudes attracted by the strengthened
370 normal flux patches in North America. From 3.0 to 2.2 cal kyr BP_{2000} the interpretation of the FCF is
371 very tricky due to the fact that the NFP at high latitudes is located between the Canadian and Siberian
372 hemispheres and the FCF values are not very significant in these times.
373 With a clockwise path at 1.8 cal kyr BP_{2000} the VGP moved quickly toward the Siberia region
374 (Siberian FCF > Canadian FCF). Then at 1.0 cal kyr BP_{2000} it reached Russia (Siberian FCF >
375 Canadian FCF), and around 0.6 cal kyr BP_{2000} it returned toward Canada (the Canadian FCF shows
376 a slight increase and the Siberian FCF decreases but it is still higher) (Fig. 8).
377 In order to test the plausibility of our hypothesis we performed a global analysis calculating the VGPs
378 from the predictions of declination and inclination given by GGF100k, CALS10k.2 and SHAWQ
379 family models at two other globally distributed locations from distant regions: the Levant region
380 (30ºN, 38ºE) and Mexico (20ºN, 99ºW). As reported in Figures 7, 8, S7, S8 the VGPs positions are
381 mostly close to the selected NFPs and mainly located in or moved toward the hemisphere with higher
382 FCF (Canadian or Siberian). Obviously, this is just an example with two locations but the results are
383 encouraging and it would be worth carrying out a deeper investigation in future.
384 Based on our analyses, we observe that the VGP motion in the polar region resembles that reported
385 for the recent magnetic pole with direct geomagnetic measurements and is mostly related to the
386 waxing and waning of radial magnetic flux lobes at CMB, preferentially located in Russia (Siberia)

and North America (Canada). However, there are other possible explanations for these motions. For example, the large VGP shift that occurred between 3.0 and 2.6 cal kyr BP_{2000}, with the VGP moving from the Barents Sea toward low latitudes and North America is coincident with a growth of radial flux in the Pacific in CALS10k.2 model. It could be that the VGP path from the NBS22.2k stack is affected by this flux more than from the LIAA, but we notice that more recent models, such as SHAWQ-Iron Age, are not consistent with this hypothesis (Figure S4 in the Supplementary Material). As a final note, it is important to take into account that VGPs are difficult to interpret in the presence of non-dipole fields. More investigation is needed and new data and global reconstructions of the geomagnetic field will provide new evidences that may confirm our results. However, with our current knowledge, our findings could be important in future perspectives on the interpretation of the VGPs.

6. Conclusion

We reconstructed the variation of the geomagnetic field during the last 22.2 cal kyr BP_{2000} on the basis of paleomagnetic and rock magnetic data from sedimentary cores collected in the Arctic region. We obtained an improved stratigraphic correlation between cores that allowed us to refine the formerly proposed age model for such sedimentary cores (Caricchi et al., 2019, 2020). Following this refinement in stratigraphic correlation and dating, we merged the paleomagnetic data from the cores in PSV and RPI stack curves (that we named the NBS22.2k stack) spanning the last 22.2 cal kyr BP_{2000}.

The NBS22.2k PSV and RPI stacks show a satisfactory match with the trends predicted at the core location by various reference global geomagnetic field models (GGF100k, CALS10k.2, SHA.DIF.14k, SHAWQ-Iron Age, SHAWQ2k) and a global RPI stack (GLOPIS-GICC05), with the exception of a few time intervals comprised between 14.1-18.4 cal kyr BP_{2000} and 14.1-17.2 cal kyr BP_{2000} for inclination and declination respectively.

412 We reconstructed the Virtual Geomagnetic Pole (VGP) path on the basis of the NBS22.2k PSV stack.
413 For the last 14 cal kyr BP_{2000}, the VGP path was overlaid on maps of the radial component of the
414 geomagnetic field at the Core-Mantle Boundary computed from the most recent geomagnetic field
415 models (GGF100k, CALS10k.2, SHAWQ-Iron Age and SHAWQ2k). Overall, we recognized
416 centuries during which the VGP position was stable and centuries during which it accelerated its
417 motion. This behavior is related to the appearance and disappearance of patches of strong radial
418 magnetic field. The more the B_r flux lobes were persistent the longer the VGP stationed in the same
419 position. We quantified this effect, calculating the Flux Concentration Factor (FCF) in Canadian and
420 Siberian hemispheres. We observed that the VGP moves toward the hemisphere with higher FCF.
421 The VGP path described both clockwise and counterclockwise trajectories moving all around the
422 Arctic region, mostly inside the surface projection of the inner core tangent cylinder. In some cases,
423 it was characterized by westward drift, in others by eastwards drift and still in others it drifted toward
424 lower latitudes, reaching Northern Europe. The largest VGP shift toward low latitudes occurred
425 between 3.0 and 2.6 cal kyr BP_{2000} and is coeval with the paleomagnetic "Levantine Iron Age
426 Anomaly" (LIAA); we associated both features to the development of a low latitude normal flux
427 patch, which acted as a VGP attractor. However, different models could provide different results
428 according to the type of data used as input, so more data are needed in order to constrain the VGP
429 trajectories.
430 Summing up, during the last 14,000 yrs the northern hemisphere was characterized by the presence
431 of transient patches of strong radial magnetic field flux patches that may have served as VGP
432 attractors driving VGP position, path and speed. The present work highlights the importance of
433 studying the variation of the geomagnetic field through the geologic past in order to improve the
434 understanding of its behavior, place in a proper historical context its recent variation and provide
435 constraints to predict its possible future evolution.

Acknowledgments

SAC thanks to Juan de la Cierva Formación Program (FJC2018-037643-I) funded by Ministerio de Ciencia e Innovación (ES). We acknowledge Captains, crews, and scientific party during the acquisition cruises SVAIS (BIO Hespérides), EGLACOM (RV OGS-Explora), CORIBAR (RV Maria S. Merian) and Eurofleets2-PREPARED (RV G.O. Sars), the Spanish projects SVAIS (POL2006-07390/CGL) and DEGLABAR (CTM2010-17386), and the Italian projects PNRA MELTSTORM and CORIBAR-IT for former sediment core analyses.

All data presented in this paper are available as supplementary materials, they are published with a DOI via GFZ Data Services (Caricchi et al., 2022 https://doi.org/10.5880.fidgeo.2022.028) and they can be downloaded from the Thematic Core Service "Multi-scale laboratories" (https://epos -msl .uu .nl /dataset) of the European Plate Observing System (EPOS) and INGV repository. Three anonymous reviewers are kindly acknowledged for the precious suggestions that highly contributed to improve the paper. We also thank Hans Thybo for the careful editorial handling.

References

1. Béguin, A., Filippidi, A., de Lange, G.J., de Groot, L.V., 2019. The evolution of the Levantine Iron Age geomagnetic Anomaly captured in Mediterranean sediments. Earth Planet. Sci. Lett. 511, 55–66. https://doi.org/10.1016/j.epsl.2019.01.021.
2. Caricchi, C., Lucchi, R.G., Sagnotti, L., Macrì, P., Morigi, C., Melis, R., Caffau, M., Rebesco, M., Hanebuth, T.J.J., 2018. Paleomagnetism and rock magnetism from sediments along a continental shelf-to-slope transect in the NW Barents Sea: implications for geomagnetic and depositional changes during the past 15 thousand years. Glob. Planet. Chang. 160, 10-27. https://doi.org/10.1016/j.gloplacha.2017.11.007.
3. Caricchi, C., Lucchi, R.G., Sagnotti, L., Macrì, P., Di Roberto, A., Del Carlo, P., Husum, K., Laberg, J.S., Morigi, C., 2019. A high-resolution geomagnetic relative paleointensity record

462 from the Arctic Ocean deep-water gateway deposits during the last 60 ky. Geochem. Geophys.
463 Geosyst. 20, 2355-2377. https://doi.org/10.1029/2018GC007955.
464 4. Caricchi C., Sagnotti L., Campuzano S.A., Lucchi R.G., Macrì P., Rebesco M., Camerlenghi
465 A., 2020. A refined age calibrated paleosecular variation and relative paleointensity stack for
466 the NW Barents Sea: Implication for geomagnetic field behavior during the Holocene. Quat.
467 Sci. Rev., 229, 106133 https://doi.org/10.1016/j.quascirev.2019.106133
468 5. Caricchi C., Campuzano S.A., Sagnotti L., Macrì P., Lucchi R.G. (2022). Paleomagnetic and
469 rock magnetic data from sedimentary core collected at high latitude (NW Barents Sea):
470 reconstructed age models and PSV - RPI stacks for the last 22 kyr. GFZ Data Services,
471 https://doi.org/10.5880.fidgeo.2022.028
472 6. Campuzano, S. A., Gómez-Paccard, M., Pavón-Carrasco, F. J., Osete, M. L. 2019. Emergence
473 and evolution of the South Atlantic anomaly revealed by the new paleomagnetic reconstruction
474 SHAWQ2k. Earth Planet. Sci. Lett., 512, 17–26. https://doi.org/10.1016/j.epsl.2019.01.050
475 7. Christensen U.R., Aubert J., Hulot G. 2010. Conditions for Earth-like geodynamo models.
476 Earth Planet. Sci. Lett. 296,487-496, https://doi.org/10.1016/j.epsl.2010.06.009.
477 8. Clark, P. U., McCabe, A. M., Mix, A. C., & Weaver, A. J. (2004). Rapid rise of sea level
478 19,000 years ago and its global implications. Science, 304(5674), 1141–1144.
479 https://doi.org/10.1126/science.1094449
480 9. Constable, C. G., Johnson, C. L., Lund S.P. 2000. Global geomagnetic field models for the
481 past 3000 years: Transient or permanent flux lobes?, Philos. Trans. R. Soc. London, Ser. A,
482 358, 991–1008.
483 10. Constable, C., Korte, M., Panovska, S., 2016. Persistent high paleosecular variation activity in
484 southern hemisphere for at least 10 000 years. Earth Planet. Sci. Lett. 453, 78e86.
485 https://doi.org/10.1016/j.epsl.2016.08.015.
486 11. Davies, C., Constable C., 2017. Geomagnetic spikes on the core-mantle boundary. Nat.
487 Commun. 8, 15593, doi: 10.1038/ncomms15593

12. Donadini, F., Korte, M., Constable, C.G., 2009. Geomagnetic field for 0-3 ka: 1. New data sets for global modeling. Geochem. Geophys. Geosyst. 10, Q06007. https://doi.org/10.1029/2008GC002295.
13. Fisher, R.A., 1953. Dispersion on a sphere. Proc. R. Soc. London, Ser. A 217, 295-305. https://doi.org/10.1098/rspa.1953.0064.
14. Hemming, S. R. (2004). Heinrich events: Massive late Pleistocene detritus layers of the North Atlantic and their global climate imprint. Reviews of Geophysics, 42, RG1005. https://doi.org/10.1029/2003RG000128
15. Jakobsson, M., Backman, J., Rudels, B., Nycander, J., Frank, M., Mayer, L., et al. 2007. The early Miocene onset of a ventilated circulation regime in the Arctic Ocean. Nature, 447(7147), 986–990. https://doi.org/10.1038/nature05924
16. Johnson C.L., Constable G.C. 1995. The time-averaged geomagnetic field as recorded by lava flows over the past 5Myr Geophys. J. Int. 122, 489-519.
17. Korte M., Holme R. 2010. On the persistence of geomagnetic flux lobes in global Holocene field models. Physics of the Earth and Planetary Interiors, 182, 179–186 doi:10.1016/j.pepi.2010.08.006
18. Korte, M., Constable, C.G., 2003. Continuous geomagnetic field models for the past 3000 years, 2003. Physics of the Earth and Planetary Interiors, 140, 73–89.
19. Korte, M., Constable, C.G., 2005. Continuous geomagnetic field models for the past 7 millennia: 2. CALS7K. Geochem. Geophys. Geosyst. 6, Q02H16. https://doi.org/10.1029/2004GC000801.
20. Korte, M., Genevey, A., Constable, C.G., Frank, U., Schnepp, E., 2005. Continuous geomagnetic field models for the past 7 millennia: 1. A new global data compilation. Geochem. Geophys. Geosyst. 6 (2) https://doi.org/10.1029/ 2004GC000800.

512 21. Korte, M., Donadini, F., Constable, C.G., 2009. Geomagnetic field for 0-3 ka: 2. a new series
513 of time-varying global models. Geochem. Geophys. Geosyst. 10, Q06008.
514 https://doi.org/10.1029/2008GC002297.
515 22. Laj C., Kissel C., 2015. An impending geomagnetic transition? Hints from the past. Front.
516 Earth Sci. 3:61. doi: 10.3389/feart.2015.0006
517 23. Livermore, P.W., Finlay, C.C, Bayliff, F., 2020. Recent north magnetic pole acceleration
518 towards Siberia caused by flux lobe elongation. Nature Geoscience, 13, 387–391.
519 https://doi.org/10.1038/s41561-020-0570-9
520 24. Lucchi, R.G., Pedrosa, M.T., Camerlenghi, A., Urgeles, R., De Mol, B., Rebesco, M., 2012.
521 Recent submarine landslides on the continental slope of Storfjorden and Kveithola trough-
522 mouth fans (north west Barents Sea). In: Yamada, Y., Kawamura, K., Ikehara, K., Ogawa, Y.,
523 Urgeles, R., Mosher, D., Chaytor, J., Strasser, M. (Eds.), Submarine Mass Movements and
524 Their Consequences, Advances in Natural and Technological Hazards Research, vol. 31.
525 Springer Science book series, pp. 735-745. https://doi.org/10.1007/978-94-007-2162-3_65.
526 25. Lucchi, R.G., Camerlenghi, A., Rebesco, M., Colmenero-Hidalgo, E., Sierro, F.J., Sagnotti,
527 L., Urgeles, R., Melis, R., Morigi, C., B_arcena, M.-A., Giorgetti, G., Villa, G., Persico, D.,
528 Flores, J.-A., Rigual-Hern_andez, A.S., Pedrosa, M.T., Macri, P., Caburlotto, A., 2013.
529 Postglacial sedimentary processes on the Storfjorden and Kveithola trough mouth fans:
530 significance of extreme glacimarine sedimentation. Glob. Planet. Chang. 111, 309-326.
531 https://doi.org/10.1016/j.gloplacha.2013.10.008.
532 26. Lucchi, R.G., Sagnotti, L., Camerlenghi, A., Macrì, P., Rebesco, M., Pedrosa, M.T., Giorgetti,
533 G., 2015. Marine sedimentary record of meltwater pulse 1a in the NW Barents Sea continental
534 margin. Arktos 1, 7. https://doi.org/10.1007/s41063-015-0008-6.
535 27. Mattingsdal, R., Knies, J., Andreassen, K., Fabian, K., Husum, K., Grøsfjeld, K., De Schepper,
536 S., 2014. A new 6 Myr stratigraphic framework for the Atlantic Arctic Gateway. Quaternary
537 Science Reviews, 92, 170–178. https://doi.org/10.1016/j.quascirev.2013.08.022

538 28. Nilsson, A., Holme, R., Korte, M., Suttie, N., Hill, M., 2014. Reconstructing Holocene
539 geomagnetic field variation: new methods, models and implications. Geophys. J. Int. 198, 229
540 - 248. https://doi.org/10.1093/gji/ggu120.
541 29. Noel, M., Batt, C.M., 1990. A method for correcting geographically separated remanence
542 directions for the purpose of archeomagnetic dating. Geophys. J. Int. 102, 753-756.
543 https://doi.org/10.1111/j.1365-246X.1990.tb04594.x.
544 30. Osete, M. L., Molina-Cardín, A., Campuzano, S. A., Aguilella-Arzo, G., Barrachina-Iba.ez,
545 A., Falomir-Granell, F., et al. 2020. Two archaeomagnetic intensity maxima and rapid
546 directional variation rates during the Early Iron Age observed at Iberian coordinates.
547 Implications on the evolution of the Levantine Iron Age Anomaly. Earth and Planetary Science
548 Letters, 533, 116047. https://doi.org/10.1016/j.epsl.2019.116047
549 31. Panovska, S., Constable, C.G., Korte, M., 2018. Extending global continuous geomagnetic
550 field reconstructions on timescales beyond human civilization. Geochem. Geophys. Geosyst.
551 19, 4757-4772. https://doi.org/10.1029/2018gc007966
552 32. Patton, H., Hubbard, A., Andreassen, K., Auriac, A., Whitehouse, P. L., Stroeven, A. P., et al.
553 2017. Deglaciation of the Eurasian ice sheet complex. Quaternary Science Reviews, 169, 148–
554 172. https://doi.org/10.1016/j.quascirev.2017.05.019
555 33. Pavón-Carrasco, F.J., Osete, M.L., Torta, J.M., Gaya-Piqué, L.R., 2009. A regional
556 archeomagnetic model for Europe for the last 3000 years, SCHA.DIF.3K: Applications to
557 archeomagnetic dating. Geochem. Geophys. 10(3), Q03013. https://doi.
558 org/10.1029/2008GC002244
559 34. Pavón-Carrasco, F. J., Osete, M. L., Torta, J. M., 2010. Regional modeling of the geomagnetic
560 field in Europe from 6000 to 1000 BC. Geochem. Geophys. 11.
561 https://doi.org/10.1029/2010GC003197

562 35. Pavón-Carrasco, F.J., Osete, M.L., Torta, J.M., De Santis, A., 2014. A geomagnetic field
563 model for the Holocene based on archeomagnetic and lava flow data. Earth Planet. Sci. Lett.
564 388, 98-109. https://doi.org/10.1016/j.epsl.2013.11.046.
565 36. Pedrosa, M., Camerlenghi, A., De Mol, B., Urgeles, R., Rebesco, M., Lucchi, R.G., shipboard
566 participants to the SVAIS and EGLACOM Cruises 2011. Seabed morphology and shallow
567 sedimentary Structure of the Storfjorden and Kveitehola trough- mouth fans (north west
568 Barents Sea). Mar. Geol. 286, 65-81. https://doi.org/10.1016/j.margeo.2011.05.009
569 37. Poirier, A., Hillaire-Marcel, C. 2011. Improved Os-isotope stratigraphy of the Arctic Ocean.
570 Geophysical Research Letters, 38, L14607. https://doi.org/10.1029/2011GL047953
571 38. Rebesco, M., Wåhlin, A., Laberg, J. S., Schauer, U., Beszczynska-Möller, A., Lucchi, R. G.,
572 et al. 2013. Quaternary Contourite drifts of the Western Spitsbergen margin. Deep Sea
573 Research Part I: Oceanographic Research Papers, 79, 156–168.
574 https://doi.org/10.1016/j.dsr.2013.05.013
575 39. Rivero-Montero M, Gómez-Paccard M., Kondopoulou D., Temac E., Pavón-Carrasco F.J.,
576 Aidona E., Campuzano S.A., Molina-Cardína A., Osete M.L., Palencia-Ortas A., Martín-
577 Hernández F., Rubat-Borel F., Venturino M., 2021. Geomagnetic field intensity changes in the
578 Central Mediterranean between 1500 BCE and 150 CE: Implications for the Levantine Iron
579 Age Anomaly evolution. Earth. Planet. Sci. Lett. Volume 557, 116732,
580 https://doi.org/10.1016/j.epsl.2020.116732
581 40. Sagnotti, L., Caricchi, C., 2018. StratFit: an excel workbook for correlation of multiple
582 stratigraphic trends. Ann. Geophys. 61, DA341. https://doi.org/10.4401/ag-7619.
583 41. Sagnotti, L., Macrì, P., Lucchi, R., Rebesco, M., Camerlenghi, A., 2011a. A Holocene
584 paleosecular variation record from the northwestern Barents Sea continental margin.
585 Geochem. Geophys. 12, Q11Z33. https://doi.org/10.1029/2011GC003810
586 42. Sagnotti, L., Smedile, A., De Martini, P.M., Pantosti, D., Speranza, F., Winkler, A., Del Carlo,
587 P., Bellucci, L.G., Gasperini, L., 2011b. A continuous palaeosecular variation record of the

588 last 4 millennia from the Augusta Bay (Sicily, Italy). Geophys. J. Int.184, 191e202.
589 https://doi.org/10.1111/j.1365-246X.2010.04860.x.
590 43. Shaar, R., Tauxe, L., Ron, H., Ebert, Y., Zuckerman, S., Finkelstein, I., Agnon, A., 2016. Large
591 geomagnetic field anomalies revealed in Bronze to Iron age arche- omagnetic data from Tel
592 Megiddo and Tel Hazor, Israel. Earth Planet. Sci. Lett. 442, 173-185.
593 https://doi.org/10.1016/j.epsl.2016.02.038.
594 44. Shaar, R., Tauxe, L., Goguitchaichvili, A., Devidze, M., Licheli, V., 2017. Further evidence
595 of the Levantine Iron Age geomagnetic anomaly from Georgian pottery. Geophys. Res. Lett.
596 26, 3-8. https://doi.org/10.1002/2016GL071494.
597 45. Shaar, R., Hassul, E., Raphael, K., Ebert, Y., Segal, Y., Eden, I., Vaknin, Y., Marco, S.,
598 Nowaczyk, N.R., Chauvin, A., Agnon, A., 2018. The first Catalog of archaeomagnetic
599 directions from Israel with 4,000 Years of geomagnetic secular variations. Front. Earth Sci. 6,
600 164. https://doi.org/10.3389/feart.2018.00164.
601 46. Turner, G.M., Thompson, R., 1981. Lake sediment record of the geomagnetic secular variation
602 in Britain during Holocene times. Geophys. J. Int. 65, 703e725.https://doi.org/10.1111/j.1365-
603 246X.1981.tb04879.x.
604 47. Wessel, P., Smith, W.H.F., Scharroo, R., Luis, J., Wobbe, F., 2013. Generic mapping tools:
605 improved Version released. EOS Trans. AGU 94 (45), 409e410. https://
606 doi.org/10.1002/2013EO450001, 2013.
607
608
609
610
611
612

Figures

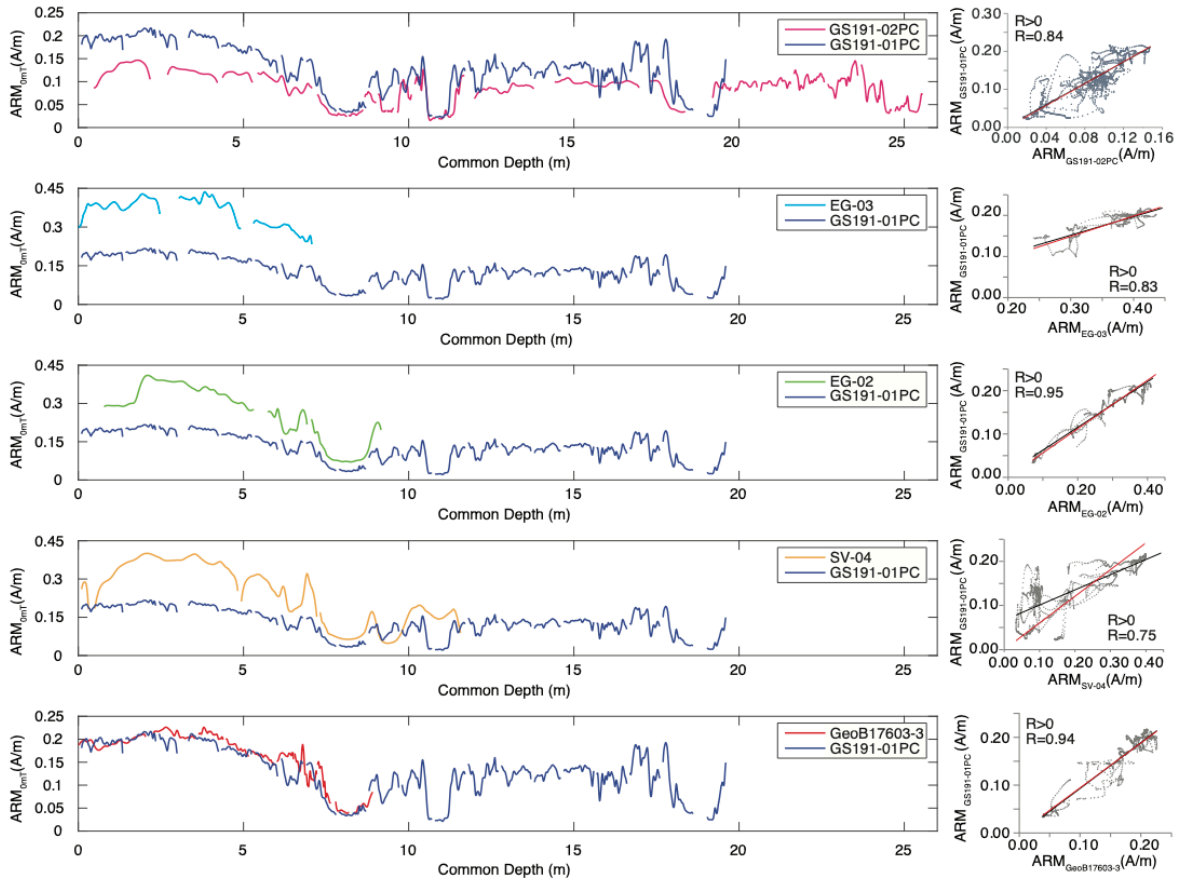

Figure 1. Correlation of the stratigraphic trends of Anhysteretic Remanent Magnetization (ARM) for the analyzed cores. GS191-01PC as the master curve and SV-04, EG-02, EG-03, GeoB17603-3 and GS191-02PC are the correlated curves (see the text for details). On the right side, the goodness of correlation is evaluated comparing the ARM values referred to a common depth. Linear fit passing through the origin ($y=ax$; red lines) and free intercept ($y=ax+b$, black lines) are shown. Correlation between GS191-01PC and GS191-02PC: $y=1.4419x$ $R^2=0.9552$, $y=1.401x+0.004$ $R^2=0.707$; Correlation between GS191-01PC and EG-03: $y=0.4958x$ $R^2=0.9926$, $y=0.4532x+0.0156$ $R^2=0.68874$; Correlation between GS191-01PC and EG-02: $y=0.5591x$ $R^2=0.9883$, $y=0.5263x+0.01$ $R^2=0.9119$; Correlation between GS191-01PC and SV-04: $y=0.6043x$ $R^2=0.8628$, $y=0.3442x+0.0665$ $R^2=0.5592$; Correlation between GS191-01PC and GeoB17603-3: $y=0.9426x$ $R^2=0.9873$, $y=0.9588x+0.0029$ $R^2=0.8919$.

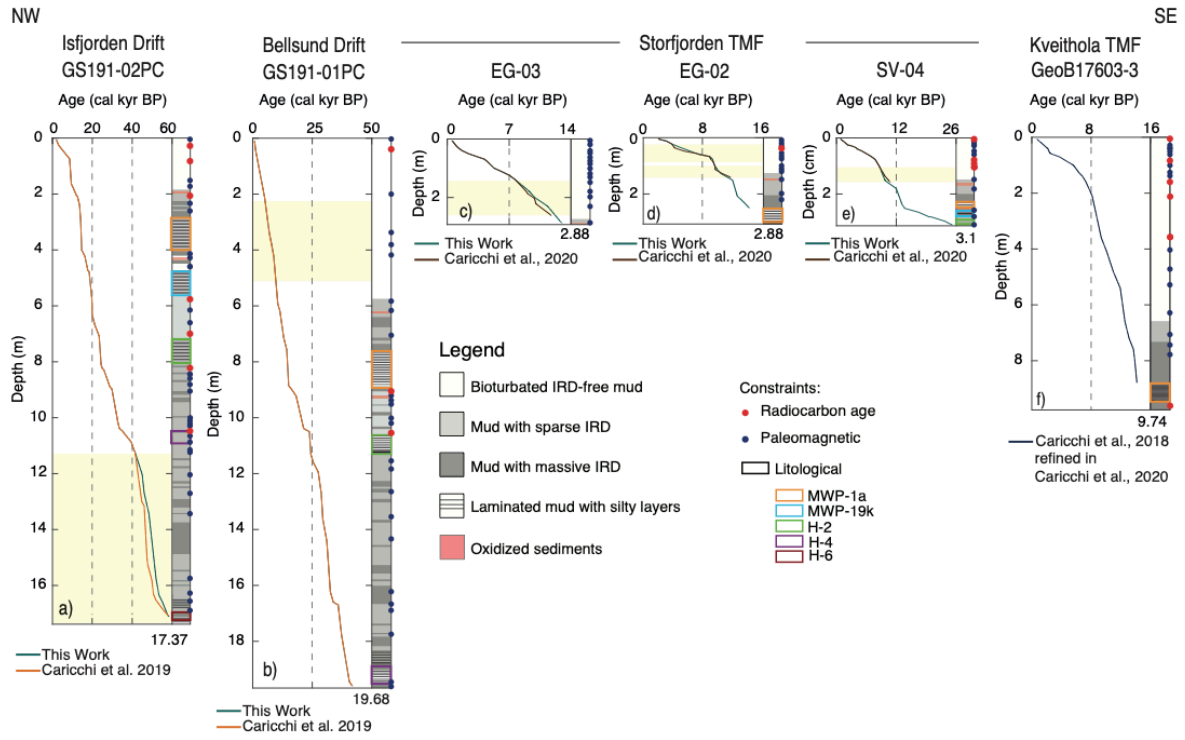

626

627 **Figure 2** Comparison between old (Caricchi et al., 2019, 2020) and refined (this work) age models
628 for the studied cores. The yellow rectangles highlight the portion of the cores where the age model
629 was refined. The red dots indicate the available radiocarbon ages, the blue dots the paleomagnetic
630 constraints and the colored rectangle the lithological constraints. Present refers to 2000 CE.
631 MWP-1a = 14.65-14.31 kyr BP; MWP-19k (MWP-1A0) = 19 kyr BP; H2= 24 kyr BP; H4= 38 kyr
632 BP; H6= ca 60 kyr BP.

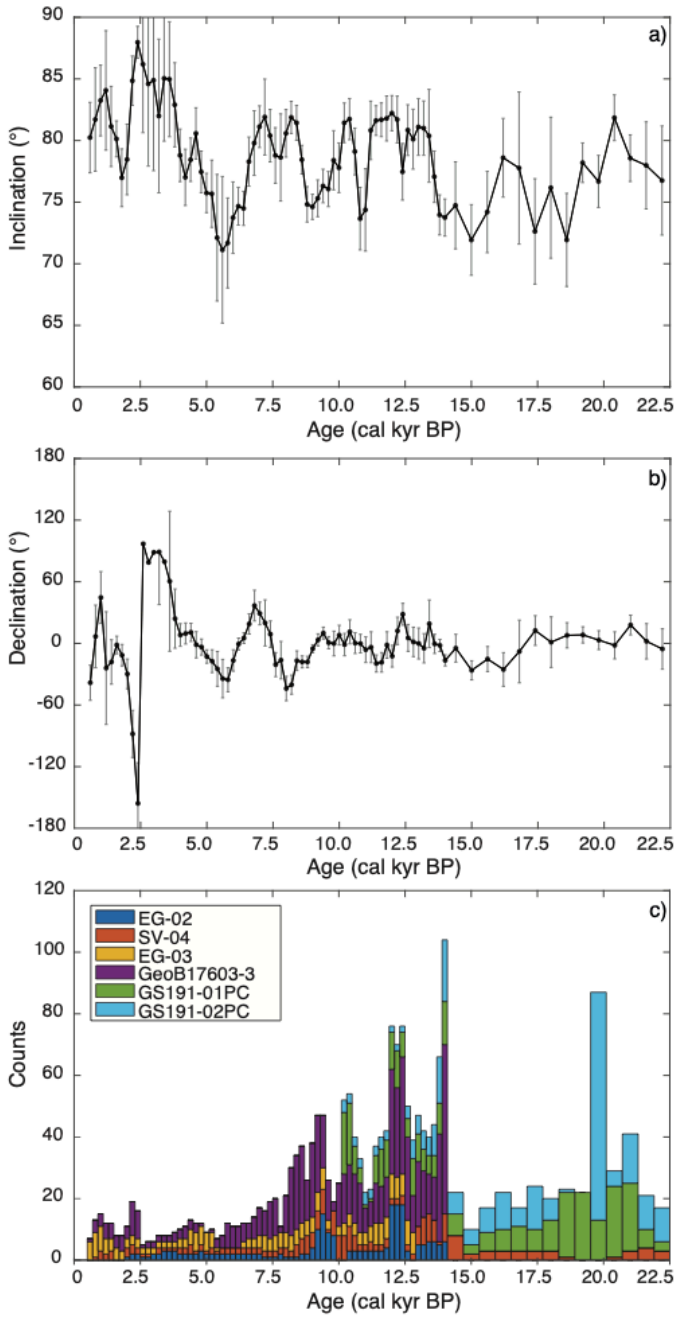

633

634 **Figure 3** The NBS22.2k stack; paleomagnetic (a) declination, (b) inclination. The black circles
635 indicate the mean value computed on data selected with a sliding window of 200 yr for the first 14
636 cal kyr BP and 600 yr for the interval between 14-22.2 cal kyr BP_{2000}. The error bars indicate the
637 standard deviations computed taking into account the whole group of data in the sliding window. (c)
638 Histogram showing the number of data across time and the various cores. Present refers to 2000 CE.

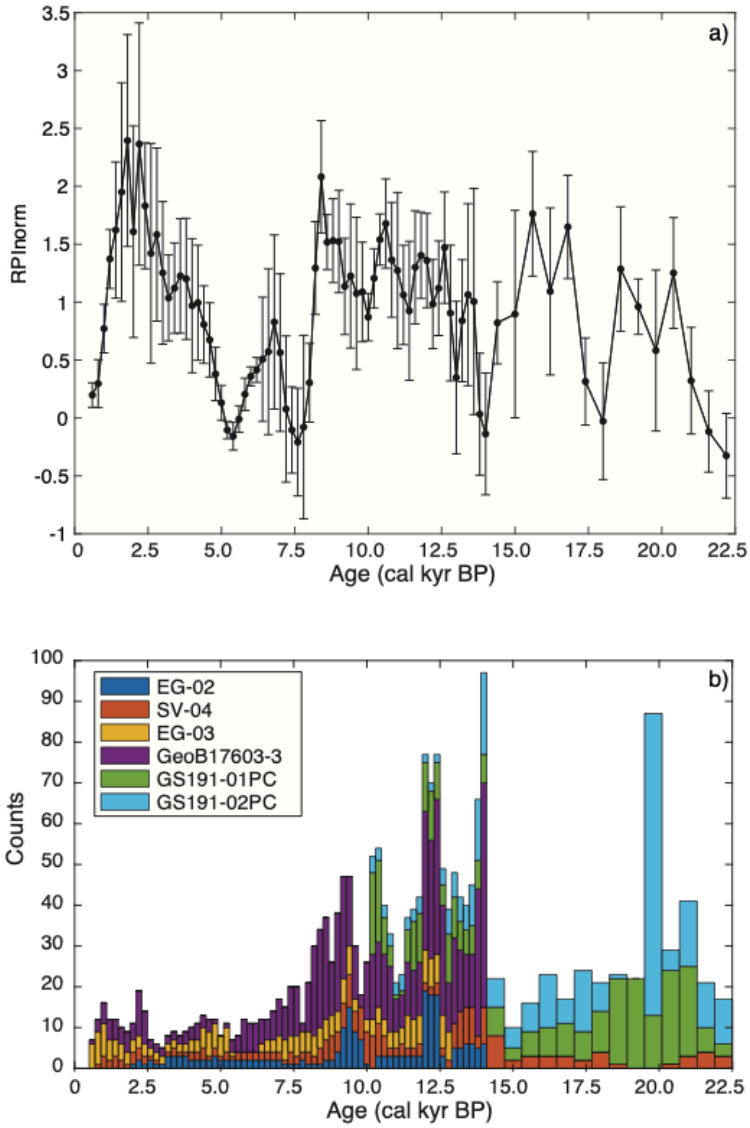

Figure 4 a) NBS22.2k RPI stack normalized to the median value according to the method reported in appendix (see Supplementary Material). The black circles indicate the mean value computed on data selected with a sliding window of 200 yr for the first 14 cal kyr BP_{2000} and 600 yr for the interval between 14-22.2 cal kyr BP_{2000}. The error bars indicate the standard deviations computed taking into account the whole group of data in each sliding window. (b) Histogram showing the number of data across time and the various cores. Present refers to 2000 CE.

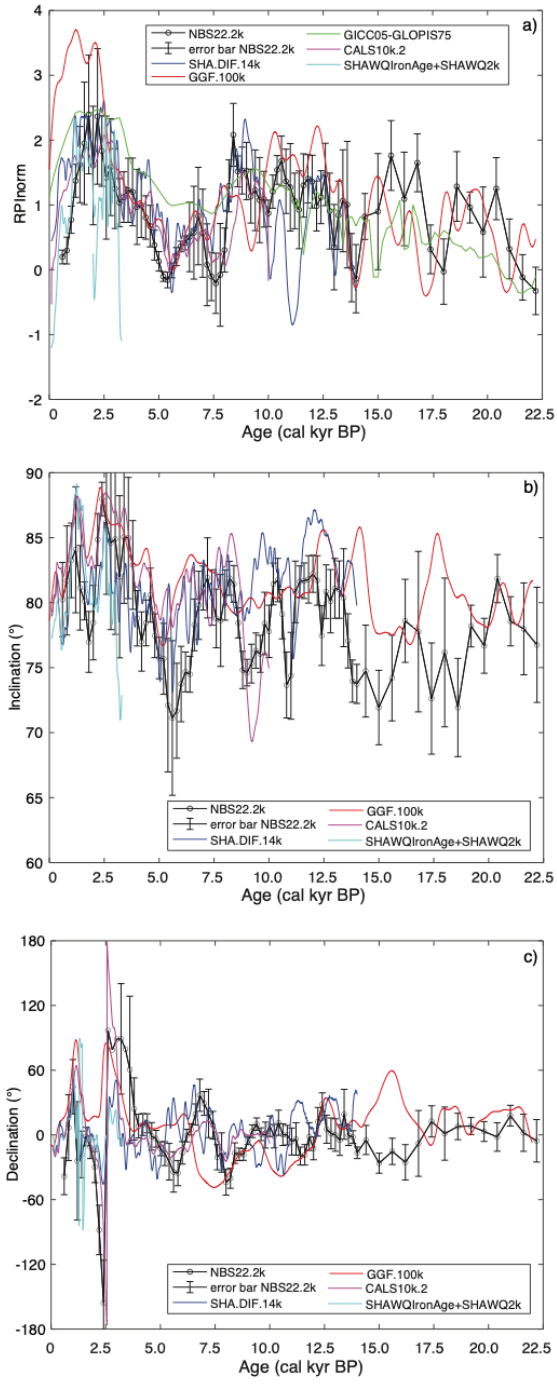

646

647 **Figure 5** Comparison of the NBS22.2k RPI and PSV stack curves with predictions from the global
648 geomagnetic field models; CALS10k.2 (Constable et al., 2016; purple curve); SHA.DIF.14k (Pavón-
649 Carrasco et al., 2014; blue curve); SHAWQ-Iron Age (Osete et al., 2020) and SHAWQ2k
650 (Campuzano et al., 2019; light blue curve); GGF100k (Panovska et al., 2018; red curve) and the
651 GICC05-GLOPIS75 stack curve (Laj and Kissel, 2015, green curve). a) RPI intensity normalized
652 median value according to the method reported in Appendix A (see supplementary material), (a)
653 paleomagnetic (b) inclination and (c) declination. The geomagnetic field models were computed at
654 the EG-03 core location, which has been selected as the reference location due to its central position
655 in the study area. The intensity values from GGF100k and GICC05-GLOPIS75 were normalized only
656 for the time period overlapping the age interval spanned by the NBS22.2k stack. Present refers to
657 2000 CE.
658

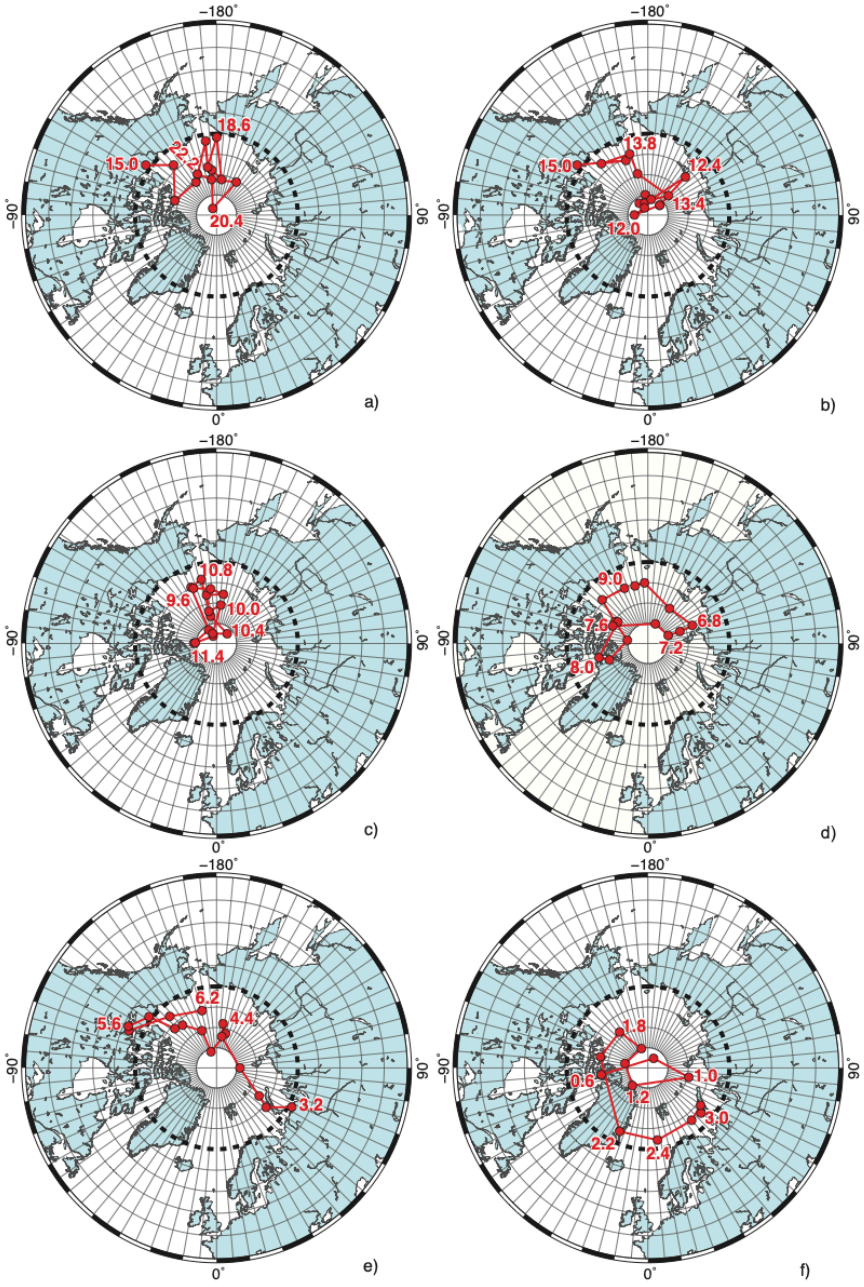
−180°
−90°
90°
0°
18.6
15.0
20.4
a)
13.8
15.0
12.4
13.4
12.0
b)
10.8
9.6
10.0
10.4
11.4
c)
9.0
7.6
6.8
7.2
8.0
d)
6.2
5.6
4.4
3.2
e)
1.8
0.6
1.0
1.2
3.0
2.2
2.4
f)

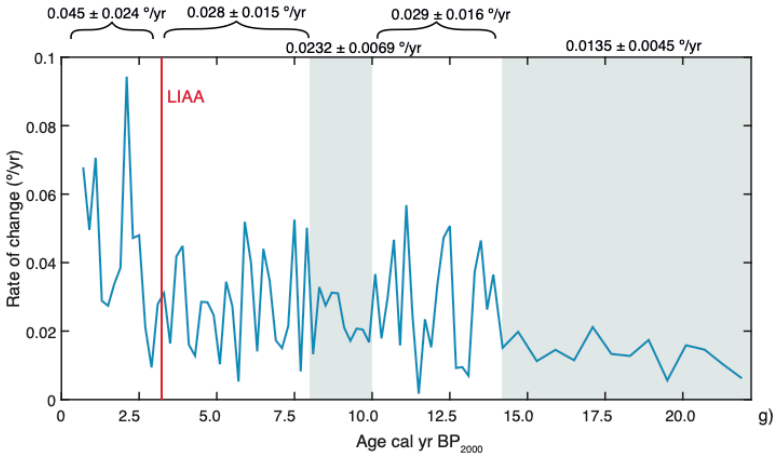
0.045 ± 0.024 °/yr
0.028 ± 0.015 °/yr
0.029 ± 0.016 °/yr
0.0232 ± 0.0069 °/yr
0.0135 ± 0.0045 °/yr
LIAA
Rate of change (°/yr)
0.1
0.08
0.06
0.04
0.02
0
0
2.5
5.0
7.5
10.0
12.5
15.0
17.5
20.0
Age cal yr BP2000
g)

Figure 6 a-f) Reconstruction of the VGP path from paleomagnetic data of the NBS22.2k PSV stack, spanning the time interval from 22.2 to 0.6 cal kyr BP_{2000}. The black dashed circle indicates the surface projection of the inner core tangent cylinder (an imaginary cylinder coaxial with Earth's rotation axis and tangential to the inner core at the equatorial plane). Numbers in plots indicate the time in cal kyr BP_{2000}. Present refers to 2000 CE. The plots have been produced by GMT 5.4.3 (Wessel et al., 2013). g) Reconstruction of the VGP rate of change for the last 22.2 cal kyr BP_{2000}.

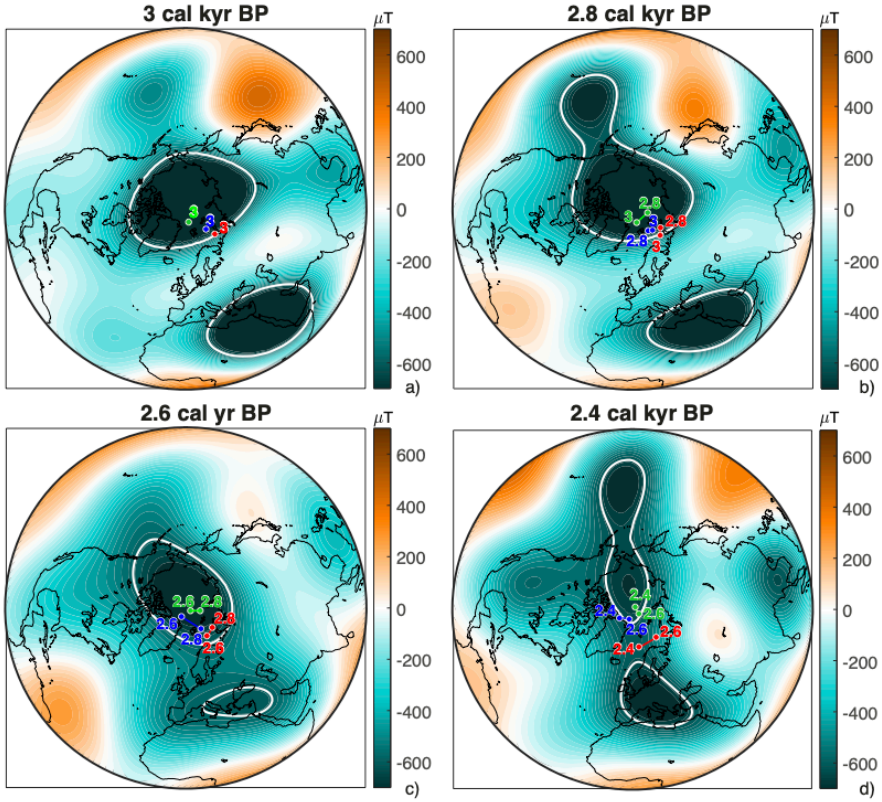

Figure 7 VGP path reconstruction of NBS22.2k PSV stack (in red), Levant (in blue) and Mexico (in green), overlaid on maps of the radial component of the geomagnetic field (in μT) at the Core-Mantle Boundary from SHAWQ-Iron Age model at (a) 3.0 cal kyr BP_{2000}, (b) 2.8 cal kyr BP_{2000}; (c) 2.6 cal kyr BP_{2000}, (d) 2.4 cal kyr BP_{2000}. Present refers to 2000 CE. White contour lines correspond to -580μT for (a-c) and -625μT for (d) and highlight the NFPs that act as VGP attractors according to our interpretation.

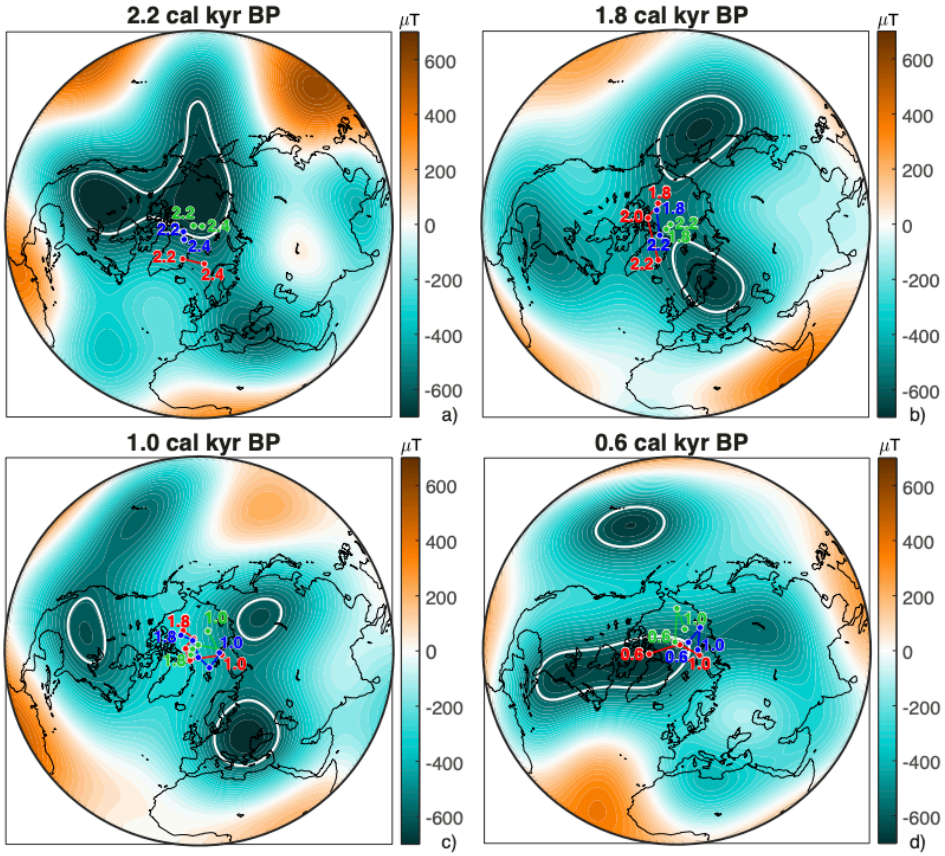

676

677 **Figure 8** VGP path reconstruction of NBS22.2k PSV stack (in red), Levant (in blue) and Mexico (in
678 green), overlaid on maps of the radial component of the geomagnetic field (in μT) at the Core-Mantle
679 Boundary from SHAWQ-Iron Age model in (a) 2.2 cal kyr BP_{2000} and SHAWQ2k in (b) 1.8 cal kyr
680 BP_{2000} (c) 1.0 kyr BP_{2000} (d) 0.6 cal kyr BP_{2000}. Present refers to 2000 CE. White contour lines
681 correspond to -625μT for (a) and -580μT for (b-d) and highlight the NFPs that act as VGP attractor
682 according to our interpretation.